





## Anisotropic charge transport in the easy-plane kagome ferromagnet Fe<sub>3</sub>Sn

Lilian Prodan <sup>1</sup>, Artem Chmeruk,<sup>2</sup> Liviu Chioncel <sup>2</sup>, Vladimir Tsurkan <sup>1,3</sup> and István Kézsmárki<sup>1</sup>

<sup>1</sup>*Experimentalphysik V, Center for Electronic Correlations and Magnetism, Institute of Physics, University of Augsburg, D-86159 Augsburg, Germany*

<sup>2</sup>*Theoretische Physik III, Institute of Physics University of Augsburg, D-86135 Augsburg, Germany and Augsburg Center for Innovative Technologies (ACIT), University of Augsburg, D-86135 Augsburg, Germany*

<sup>3</sup>*Institute of Applied Physics, Moldova State University, MD 2028 Chisinau, Republic of Moldova*

 (Received 31 May 2024; revised 23 July 2024; accepted 21 August 2024; published 5 September 2024)

We report on the anisotropic electronic properties of the metallic kagome ferromagnet Fe<sub>3</sub>Sn, as revealed by magnetotransport studies on single-crystalline samples and material-specific *ab initio* calculations. The longitudinal resistivity shows a remarkable anisotropy, where surprisingly the resistivity perpendicular to the kagome planes ( $\rho_{zz}$ ) is about three times lower than the in-plane resistivity ( $\rho_{xx}$ ). The ordinary Hall constants are negative for the magnetic field applied parallel to the  $\mathbf{H}||\mathbf{c}$  and positive for  $\mathbf{H}||\mathbf{a}$ , indicating the coexistence of electron- and hole-like carriers at the Fermi surface. The anomalous Hall resistivity ( $\rho_{ij}^A$ ) shows large values over a wide temperature range and exhibits a significant anisotropy ratio ( $\rho_{xy}/\rho_{zy}$ ), with  $\rho_{xy} = 8 \mu\Omega \text{ cm}$  and  $\rho_{zy} = 3.2 \mu\Omega \text{ cm}$  at room temperature. Our study reveals that the anisotropy ratio scales almost linearly with the magnetocrystalline anisotropy constant ( $K_u$ ) over a broad temperature range ( $2 \text{ K} \leq T \leq 300 \text{ K}$ ), indicating that spin-orbit coupling is the underlying mechanism driving both the anisotropic transport properties and the magnetocrystalline anisotropy energy. Material-specific *ab initio* calculations further demonstrate that the magnetic reconstruction of bands near the Fermi level, induced by the spin-orbit coupling, is predominantly responsible for the anisotropic behavior of the Berry curvature and, consequently, the large anomalous Hall effect observed in Fe<sub>3</sub>Sn. These results provide valuable insight into the complex interplay between charge transport and magnetism in kagome magnets, emphasizing the strong manifestation of spin-orbit coupling on kagome lattices.

DOI: [10.1103/PhysRevB.110.094407](https://doi.org/10.1103/PhysRevB.110.094407)

### I. INTRODUCTION

Correlated kagome magnets, extensively investigated as possible candidates of quantum spin-liquid [1,2], have recently been recognized as a versatile platform to investigate the interplay between the topology of the electronic band structure and magnetism [3–7]. The ability of the kagome lattice to host magnetic ions with various spin and orbital degrees of freedom also offers a large flexibility in the experimental realization of these novel states. The most prominent topological phenomena recently discovered in materials with kagome structure are: topological superconductivity [8], the Lifshitz transition [9], the anomalous Hall effect (AHE) in antiferromagnets [10,11], giant anomalous Hall, Nernst, and magneto-optical effects in ferromagnets [12–17], spin-ice state [18], and skyrmionic bubbles [19–21].

Spin-orbit coupling (SOC) has long been established to play a crucial role in the magnetic and electronic properties of kagome magnets [4,22,23]. SOC governs the anisotropic behavior of the magnetization and also influences the charge and thermal transport [15,24]. Band-structure calculations have demonstrated that SOC can modify the dispersion of energy bands, particularly strongly affecting bands near linear band crossings, such as nodal points and nodal lines [4,17]. Subsequently, an enhancement of the Berry curvature takes place resulting in a giant transverse charge and thermal transport [24]. Very recent observations of large anomalous

Hall and Nernst effects in kagome magnets like Co<sub>3</sub>Sn<sub>2</sub>S<sub>2</sub> [12,17,25], Mn<sub>3</sub>Sn [26], Fe<sub>3</sub>Sn [15], and Fe<sub>3</sub>Sn<sub>2</sub> [13,16] were assigned to have a topological origin. The nontrivial band topology was also invoked for explanation of the giant “anomalous” anisotropy of the longitudinal conductivity discovered in the paramagnetic kagome metal CoSn, where the interplane conductivity is by a factor of 60 higher than the in-plane conductivity [27]. Here, the term “anomalous” is used to distinguish it from the conventional anisotropy of the conductivity of quasi-2D layered materials, where the interplane conductivity is significantly lower than the in-plane conductivity [28–31]. It is worth to mention that the “anomalous” anisotropy of the longitudinal conductivity was recently found also in several other kagome magnetic metals [10,18,27,32–35]. However, the “anomalous” conductivity anisotropy observed in kagome metals is not yet well understood.

In addition to the anisotropy of the longitudinal conductivity, the anisotropy of AHE was also widely studied in antiferromagnets with chiral spin structure Mn<sub>3</sub>X [10,11,36,37] and rare-earth kagome magnets RMn<sub>6</sub>Sn<sub>6</sub> [30,38]. Significant anisotropy in the anomalous Hall resistivities,  $\rho_{xy}^A/\rho_{zy}^A$ , was also recently reported for related kagome ferromagnet Fe<sub>3</sub>Sn<sub>2</sub> and hexagonal noncollinear magnet Fe<sub>5</sub>Sn<sub>3</sub> [33,39]. The origin of the anisotropy of the anomalous Hall effect in metallic kagome magnets is still an open issue.

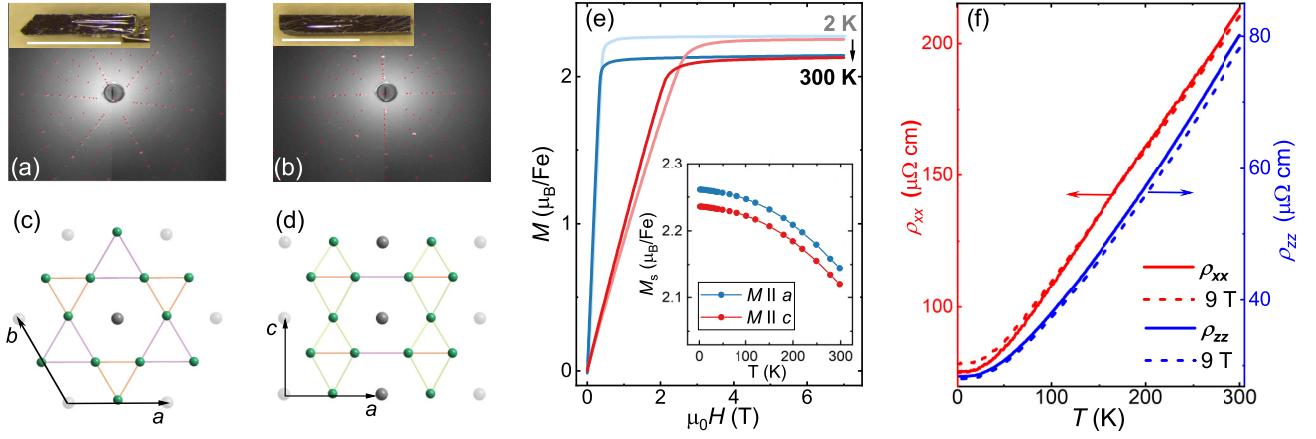


FIG. 1. Optical images and Laue x-ray diffraction patterns of the  $ab$  (a) and  $ac$  planes (b) of  $\text{Fe}_3\text{Sn}$  single crystals. White lines correspond to the scale of 1 mm. (c) Breathing kagome lattice of Fe triangles of two distinct sizes (marked by orange and purple colors) with Sn atoms located at the center of Fe hexagons. (d) Location of the Fe and Sn atoms in the  $ac$  plane. Fe atoms are colored in green, while Sn atoms within and out of the unit cell are colored in grey and light gray, respectively. (e) Magnetization curves measured at 2 K (transparent colors) and 300 K (bold colors) in magnetic fields applied along the  $a$  and  $c$  axes. The inset shows the magnetization in 7 T for different temperatures. (f) Temperature dependence of the longitudinal resistivity  $\rho_{xx}$  (red, left axis) and  $\rho_{zz}$  (blue, right axis) for single-crystalline  $\text{Fe}_3\text{Sn}$ . The dashed lines show the resistivity data in 9 T.

Here we focus on the anisotropy of charge transport, both in terms of the longitudinal and transverse conductivity, in the ferromagnetic kagome metal  $\text{Fe}_3\text{Sn}$ . It crystallizes in a hexagonal structure, with space group  $P6_3/mmc$ , in which Fe ions form a kagome lattice in the  $ab$  plane, while Sn ions occupy the center of the hexagon [see Fig. 1(c)]. The primitive unit cell of  $\text{Fe}_3\text{Sn}$  is composed of kagome bilayers stacked along the  $c$  axis, Fig. 1(d). Strong spin-orbit coupling in  $\text{Fe}_3\text{Sn}$  is manifested via significant easy-plane magnetocrystalline anisotropy [40]. The first anisotropy constant  $K_1$  has a value of  $-1.3 \times 10^6 \text{ J/m}^3$  at 2 K, which is the largest among the Fe-Sn ferromagnets. Moreover, based on such strong magnetocrystalline anisotropy, the DFT band-structure calculations predicted an anomalous Hall conductivity (AHC)  $\sigma_{xy}^A = 757 \Omega^{-1} \text{ cm}^{-1}$  for  $\text{Fe}_3\text{Sn}$  to be also the largest among the Fe-Sn family [41].

The first experimental Hall effect reported by Chen *et al.* [15] on polycrystalline sample  $\text{Fe}_{2.97}\text{Sn}_{1.03}$  (with Fe deficiency) indeed revealed large anomalous Hall conductivity  $\sigma_{ij}^A \approx 500 \Omega^{-1} \text{ cm}^{-1}$  (at 200 K) as an average over the in-plane and interplane orientation. The DFT calculations of AHC were in good agreement with the experimental data. The large intrinsic AHC in  $\text{Fe}_3\text{Sn}$  was suggested to originate from the nodal plane producing Berry curvature enhanced along the hexagonal frame near the Fermi level [15]. Belbase *et al.* [42] recently reported the Hall effect on a single-crystalline sample measured in conventional configuration with current  $\mathbf{I} \parallel \mathbf{a}$  and magnetic field  $\mathbf{H} \parallel \mathbf{c}$ . They obtained a value of  $\sigma_{xy}^A \approx 500 \Omega^{-1} \text{ cm}^{-1}$  at 200 K. Their DFT calculations revealed the Weyl nodes near the Fermi energy and yielded for the intrinsic AHC values of  $\sigma_{xy}^A \approx 702 \Omega^{-1} \text{ cm}^{-1}$  and  $\sigma_{yz}^A \approx 482 \Omega^{-1} \text{ cm}^{-1}$ . Low *et al.* [43] measured the Hall effect on a single-crystalline sample  $\text{Fe}_{2.98}\text{Sn}$  (with deficit of Fe) in configuration  $\mathbf{I} \parallel \mathbf{c}$ ,  $\mathbf{H} \parallel \mathbf{a}$ , and reported a value of  $\sigma_{zx}^A = 425 \Omega^{-1} \text{ cm}^{-1}$  at 250 K. From the analysis of the anomalous Hall conductivity they estimated the value of the intrinsic

AHC to be  $\sigma_{zx}^A = 425 \Omega^{-1} \text{ cm}^{-1}$ , which is close to  $\sigma_{zx}^A$  resulting from the DFT calculations of Belbase *et al.* The authors also noted that, at low temperatures, the extrinsic contribution to the AHE as a result of skew scattering is comparable to the intrinsic AHE.

In this study we investigate experimentally the charge transport properties of single-crystalline  $\text{Fe}_{3+\delta}\text{Sn}_{1-\delta}$  ( $\delta = 0.02; 0.03$ ) measured for different configurations and compare our results with those reported in Refs. [15,42,43]. We uncovered anisotropy in the longitudinal conductivities and anomalous Hall effect in  $\text{Fe}_3\text{Sn}$ . In addition, our band-structure calculations reveal the anisotropy in the Berry curvature distribution for different magnetization directions.

## II. METHODS

### A. Experimental details

$\text{Fe}_3\text{Sn}$  single crystals have been grown using the chemical transport reactions method using iodine as a transport agent [40]. Well-shaped rectangular samples with dimensions up to 2 mm along the largest side were obtained [see Figs. 1(a) and 1(b)]. The chemical composition of the samples was checked by energy dispersive x-ray spectroscopy (EDS) analysis utilizing the ZEISS Crossbeam 550 system. The average concentration of Fe and Sn, measured for 10 samples from the same batch, yields a composition of  $\text{Fe}_{3.00(1)}\text{Sn}_{0.98(1)}$ . The composition of the two largest samples selected for transport measurements,  $\text{Fe}_{3.03}\text{Sn}_{0.97}$  (S1,  $\rho_{xx}$ ) and  $\text{Fe}_{3.02}\text{Sn}_{0.98}$  (S2,  $\rho_{zz}$ ), revealed slight excess of Fe. The crystal orientation was checked by the Laue x-ray diffraction [see Figs. 1(a) and 1(b)].

The magnetic properties of S1 and S2 were studied by the SQUID magnetometer (MPMS 3, Quantum Design) in the temperature range 2–300 K and magnetic fields up to 7 T. The main panel of Fig. 1(d) shows the magnetization curves measured at 2 K and 300 K for two main crystallographic axes,  $\mathbf{M} \parallel \mathbf{a}$  and  $\mathbf{M} \parallel \mathbf{c}$ , respectively. The inset of Fig. 1(d)

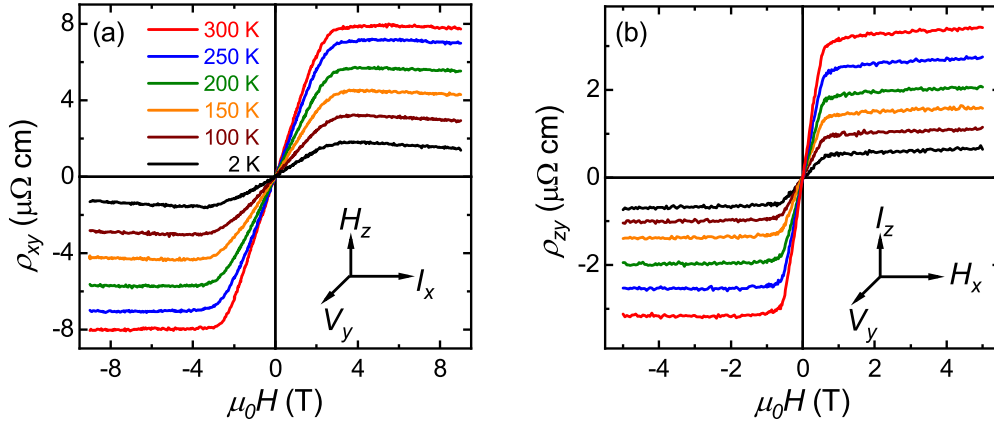


FIG. 2. Field dependencies of the Hall resistivities  $\rho_{xy}$  (a) and  $\rho_{zy}$  (b) measured at different temperatures for single-crystalline  $\text{Fe}_{3+\delta}\text{Sn}_{1-\delta}$ . The color code is valid for both configurations. Insets in the right bottom corners show the measurement configuration with respect to applied current  $I_i$ , magnetic field  $H_k$  and measured Hall voltage  $V_j$ .

shows the temperature dependence of magnetization in 7 T for samples S1 ( $\mathbf{M}||\mathbf{a}$ ) and S2 ( $\mathbf{M}||\mathbf{c}$ ). The hysteresis curves and magnetization in 7 T reproduce well the data reported in Ref. [40].

Transport properties were investigated by the four-probe method using the resistivity option of the PPMS system (Quantum Design) at temperatures between 2 and 300 K in magnetic fields up to 9 T. Current and potential contacts were made with silver paint. The ratio of length to lateral size of samples was larger than three, which eliminates the shunting effect of the current contacts [44] that is inevitably present in the measurements on samples of small size. A current of  $\mathbf{I} = 5$  mA (with an excitation frequency of 8 Hz) was applied in the kagome  $ab$ - ( $\mathbf{I}||\mathbf{a}$ ,  $\rho_{xx}$ ) and inter  $ac$  planes ( $\mathbf{I}||\mathbf{c}$ ,  $\rho_{zz}$ ) of the respective samples. Hall resistivity  $\rho_{ij}$  was measured for three different configurations: (i)  $\rho_{xy}$  with  $\mathbf{I}||\mathbf{a}$ ,  $\mathbf{H}||\mathbf{c}$ ; (ii)  $\rho_{zx}$  with  $\mathbf{I}||\mathbf{c}$ ,  $\mathbf{H} \perp \mathbf{a}$ , and (iii)  $\rho_{zy}$  with  $\mathbf{I}||\mathbf{c}$ ,  $\mathbf{H}||\mathbf{a}$ . The coordination for Hall resistivity was chosen such that  $i$  and  $j$  show the directions of the applied current and measured Hall voltage on the orthogonal basis  $x$ ,  $y$ ,  $z$ , where the  $x$  and  $z$  axes are parallel to the crystallographic  $\mathbf{a}$  and  $\mathbf{c}$  axes, while the  $y$  axis is perpendicular to both (see inset of Fig. 2).

### B. Computational details

We calculate the AHC and the corresponding Berry curvature using a three-step procedure, as described below. First, the electron density is obtained within the framework of density functional theory (DFT) [45,46]. All DFT calculations were performed using projector-augmented plane wave method (PAW) [47] as implemented in the VASP (version 6.4.2) code [48,49]. The valence states were  $4s^13d^73p^{10}$  for Fe, and  $5s^25p^2$  for Sn, respectively. The  $3p$  states in Fe were treated as semi-core, and  $4d$  in Sn were kept frozen in the core. The exchange-correlation term in the effective Kohn-Sham potential was approximated according to the Perdew-Burke-Ernzerhof parametrization for solids (PBEsol) of the generalized gradient approximation (GGA) [50]. The plane-wave kinetic energy cutoff was 400 eV and convergence of the self-consistent cycle was assumed when the total energy changes were less than  $10^{-8}$  eV. We use experimentally

obtained lattice parameters from Ref. [40]. The integration in the Brillouin zone (BZ) was done on a  $12 \times 12 \times 12$   $\Gamma$ -centered grid. Smaller  $\mathbf{k}$  grids were not able to achieve convergence. The ferromagnetic state with the magnetization along the  $\mathbf{c}$  axis was modeled by initializing the local magnetic moments on Fe site along the  $\mathbf{c}$  axis and on Sn site in the opposite direction. The same was done for the magnetization along the  $\mathbf{a}$  axis. Both cases were studied with and without SOC.

Next, we construct a tight-binding model (TB) using the wannierization procedure [51] as implemented in Wannier90 toolkit [52]. The Kohn-Sham states were projected on a set of Wannier functions (WF). The basis set for the construction of the WFs was composed of  $p_x$ ,  $p_y$ ,  $p_z$ ,  $d_{xy}$ ,  $d_{yz}$ ,  $d_{xz}$ ,  $d_{z^2}$ ,  $d_{x^2-y^2}$  orbitals on Fe site, and  $s$ ,  $p_x$ ,  $p_y$ ,  $p_z$  orbitals on Sn site, respectively. This resulted in the overall number of 112 WFs. The quality of the obtained WFs was checked by examining the band structure of our TB model against the bare bands from DFT as well as the other available DFT results [42]. We found the resulting TB band structure to be in a very close match with both DFT band structures, indicating a reliable quality of the constructed WFs.

Last, we calculate the AHC and Berry curvature using Wanniertools software package [53]. The AHC was calculated by Wannier interpolation on a  $151 \times 151 \times 151$  mesh [54]. Different components of the Berry curvature  $\Omega^\gamma(\mathbf{k})$  ( $\gamma = \{x, y, z\}$ ) were studied by examining their distribution in different  $(k_x, k_y)$  planes in the BZ for various constant  $k_z$  values. These calculations were performed on a  $221 \times 221 \times 1$   $\mathbf{k}$  grid. Changing the grids for AHC and Berry curvature calculations for slightly more or less dense showed essentially no changes to the results.

## III. RESULTS AND DISCUSSION

### A. Longitudinal resistivity

The temperature dependence of the longitudinal resistivity  $\rho_{xx}$  and  $\rho_{zz}$  are shown in Fig. 1(e). Both in-plane  $\rho_{xx}$  and interplane  $\rho_{zz}$  resistivities have a metal-like temperature dependence and residual resistivity ratio (RRR)  $\rho_{300\text{K}}/\rho_{2\text{K}} \approx 3$ ,

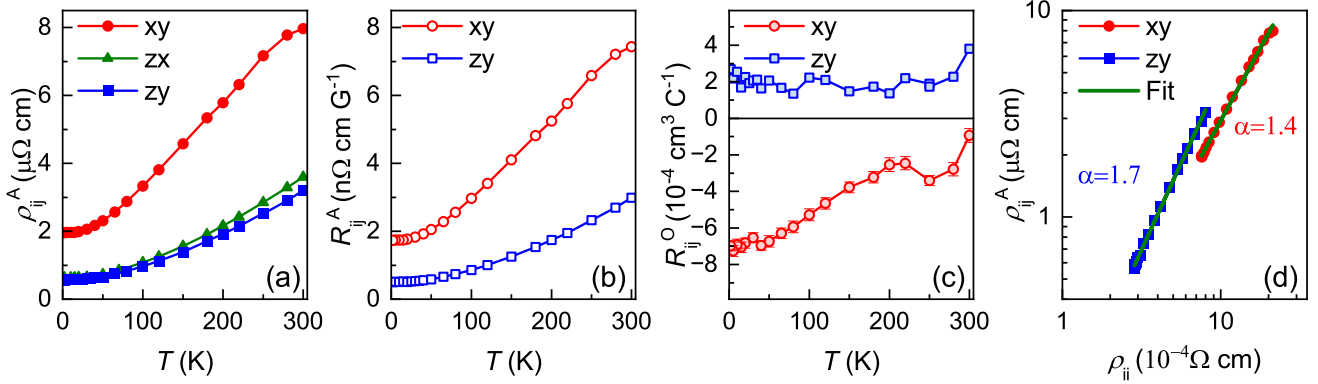


FIG. 3. Temperature dependence of the anomalous Hall resistivity  $\rho_{ij}^A$  (a), anomalous Hall coefficient  $R_{ij}^A$  (b), and ordinary Hall coefficient  $R_{ij}^O$  (c) calculated for different configurations in single-crystalline  $\text{Fe}_{3+\delta}\text{Sn}_{1-\delta}$ . (d) Logarithmic plot of off-diagonal  $\rho_{ij}^A$  and longitudinal  $\rho_{ii}^A$  resistivity. The  $\alpha$  values represent the slope of linear fit.

similar to those reported in Refs. [42,43] and for the interplane resistivity in  $\text{Fe}_3\text{Sn}_2$  [33]. We found that the interplane resistivity is significantly lower than the resistivity in the kagome plane that seems to be counterintuitive for a kagome layer-based system and will be discussed later. The temperature dependence of the resistivity was fitted by  $\rho_{ii} - \rho_{ii0} = \alpha \times T^n$ , where  $\rho_{ii0}$  is the residual resistivity. For  $\rho_{xx}$ , we determined the values of the power exponent  $n = 2.1(1)$  for temperatures below 60 K and  $1.2(1)$  at temperatures above 200 K. Larger values of  $n$  were obtained for  $\rho_{zz}$ ,  $2.5(1)$  and  $1.5(1)$ , respectively. The exponent at low temperatures suggests Fermi-liquid behavior and gradual change towards electron-phonon scattering at high temperatures. The essential difference between the exponents for  $\rho_{xx}$  and  $\rho_{zz}$  indicates distinct transport mechanisms along these two directions.

The application of a magnetic field perpendicular to  $\mathbf{I}$  (transverse magnetoresistance) has a minor effect on the resistivity for both configurations [dashed lines in Fig. 1(e)]: the magnetoresistance is less than 2% in a field of 9 T at 300 K. Interestingly, at high temperatures the magnetoresistance has a negative sign for both directions, while at low temperatures it changes to positive only for the in-plane configuration. The change of sign of magnetoresistance has previously been observed in similar kagome materials such as  $\text{Fe}_3\text{Sn}_2$  [55,56] and elemental  $3d$  ferromagnets [57]. This effect has been attributed to the interplay between magnetic scattering at high temperatures and the dominant role of the Lorentz force on carrier motion at low temperatures. This observation once again indicates the competition between two effects in the charge transport of  $\text{Fe}_3\text{Sn}$  in different temperature regimes.

## B. Hall resistivity

Further, we discuss the Hall resistivity  $\rho_{ij} = V_j d / I_i$ , which is calculated from the measured Hall voltage  $V_j$  generated by the magnetic field  $H_k$  applied transversely to the current  $I_i$  in a sample with thickness  $d$ . In ferromagnetic compounds the Hall resistivity is described as  $\rho_{ij} = \rho_{ij}^O + \rho_{ij}^A = R_O H + R_A M$ . Here,  $\rho_{ij}^O$  is the ordinary Hall resistivity,  $\rho_{ij}^A$  is the anomalous Hall resistivity, while  $R_O$  and  $R_A$  are the ordinary and anomalous Hall coefficients,  $H$  is the applied magnetic

field and  $M$  is the magnetization. The absolute accuracy of our measurements is  $\sim 10\%$ .

The prominent feature of the Hall effect revealed by our study is the anisotropic behavior of the anomalous Hall resistivity  $\rho_{ij}^A$ . We found that the Hall resistivity  $\rho_{xy}$  saturates in fields above 3 T, while  $\rho_{zx}$  and  $\rho_{zy}$  above 1 T [Figs. 2(a) and 2(b)]. The saturation fields of the AHE match with those in the magnetization and reflect the strong easy-plane anisotropy of  $\text{Fe}_3\text{Sn}$  [40]. The anomalous Hall resistivities calculated by extrapolation of the data from the high fields to  $H = 0$  show a ratio of  $\rho_{xy}^A / \rho_{zy}^A$  of about 2.5 at room temperature, which increases up to 3.5 down to 2 K, Fig. 6(a) below. Namely, at 300 K the calculated anomalous Hall resistivities are  $\rho_{xy}^A = 8 \mu\Omega \text{ cm}$ ,  $\rho_{zy}^A = 3.2 \mu\Omega \text{ cm}$ , and  $\rho_{zx}^A = 3.6 \mu\Omega \text{ cm}$ . The temperature dependencies of the anomalous Hall resistivities  $\rho_{xy}^A$ ,  $\rho_{zx}^A$ , and  $\rho_{zy}^A$  are shown in Fig. 3(a). The difference between the out-of-plane Hall resistivities,  $\rho_{zx}$  and  $\rho_{zy}$ , is within the measurement accuracy.

The anomalous Hall coefficients  $R_{ij}^A = \rho_{ij}^A / M$  were calculated using the experimental magnetization at saturation for both  $(\mathbf{M} \parallel \mathbf{a})$  and  $(\mathbf{M} \parallel \mathbf{c})$  orientations [see Fig. 3(b) and inset of Fig. 1(e)]. Similar to anomalous Hall resistivities, the anomalous Hall coefficients  $R_{xy}^A$  and  $R_{zy}^A$  also exhibit significant anisotropic effects, with a ratio of approximately 3.4 at 2 K and 2.2 at 300 K. Note that the nonzero values of  $R_A$  at 2 K suggest noticeable extrinsic contribution to the AHE related to disorder and impurities, which in our case dominates in the kagome plane.

Interestingly, we found that the ordinary Hall effect has a different sign for the two configurations: negative for  $\rho_{xy}$  and positive for  $\rho_{zx}$  and  $\rho_{zy}$ . This implies the coexistence of both electron and hole charge carriers, where electrons dominate for the  $\mathbf{I} \parallel \mathbf{a}$ , and holes dominate for  $\mathbf{I} \parallel \mathbf{c}$ . The ordinary Hall coefficient  $R_O$  was calculated from the slope of the high-field part of the Hall isotherm in fields far above magnetic saturation (in the field range 6–9 T for  $\rho_{xy}$  and 3–5 T for  $\rho_{zx}$  and  $\rho_{zy}$ ). For in-plane transport, the ordinary Hall coefficient  $R_{xy}^O$  has a negative sign, Fig. 3(c). At 2 K, the value of  $R_O$  corresponds to electron concentration of  $9 \times 10^{21} \text{ cm}^{-3}$  and is close to  $1.2 \times 10^{22} \text{ cm}^{-3}$  reported in Ref. [42] for the sample with a similar orientation. With increasing temperature, the absolute value of  $R_O$  decreases and tends to change sign at temperatures



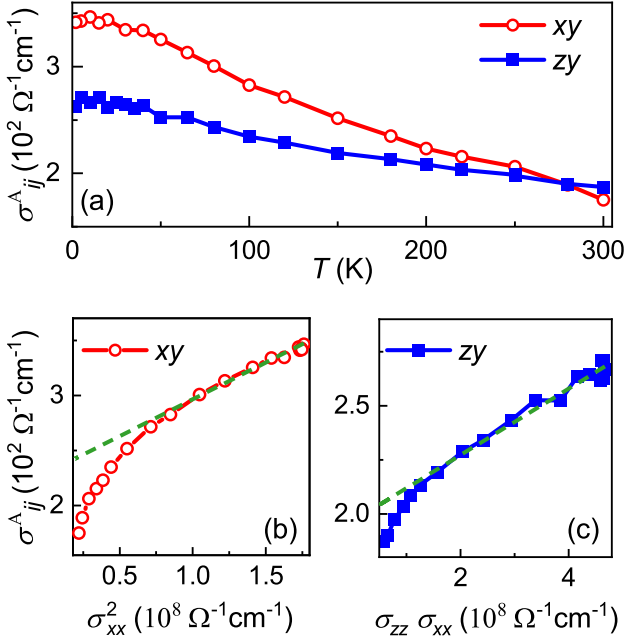


FIG. 4. (a) Temperature dependence of the anomalous Hall conductivity  $\sigma_{ij}^A$  calculated for two directions.  $\sigma_{ij}^A$  vs longitudinal conductivity  $\sigma_{xx}^2$  for the in-plane (b) and interplane  $\sigma_{zz}\sigma_{xx}$  (c) configurations. The dashed-green lines show the extrapolation of the low-temperature part of AHC.

above 300 K. It differs from Ref. [42], where the sign change of  $R_O$  was found to take place around 200 K. The ordinary Hall coefficient  $R_{zy}^O$  for the out-of-plane transport has a positive sign and is almost temperature independent. Its value corresponds to the hole concentration of  $3 \times 10^{22} \text{ cm}^{-3}$ , similar to that reported in Ref. [43] for the same orientation. Band-structure calculations show that various bands cross the Fermi energy in  $\text{Fe}_3\text{Sn}$ . This is likely reflected in the different signs of the ordinary Hall coefficient, as a consequence of the different curvatures of the bands at the Fermi level, i.e., the coexistence of electron- and hole-like carriers at the Fermi surface. Similar observation was recently reported for  $\text{Fe}_3\text{Sn}_2$  [33].

Figure 3(d) shows the logarithmic plot of  $\log(\rho_{ij}) = f[\log(\rho_{ii})]$  revealing a slope  $\alpha \approx 1.4$  for  $\mathbf{I}||\mathbf{a}$  and 1.7 for  $\mathbf{I}||\mathbf{c}$ . The large difference in the value of the exponent  $\alpha$  in the later case indicates that the contribution of the quadratic term related to the Berry curvature and/or side-jump mechanisms is larger for the interplane transport.

The anomalous Hall conductivity  $\sigma_{ij}^A$  is calculated according to the expression  $\sigma_{ij}^A = -\rho_{ij}^A / [(\rho_{ii}\rho_{jj} + (\rho_{ij}^A)^2)]$ . As a consequence of symmetry  $\rho_{yy} = \rho_{xx}$ , and  $\rho_{yy} \neq \rho_{zz}$ . For convenience we plot in Fig. 4(a) the  $|\sigma_{ij}^A|$  as function of the temperature. Note that our data analysis uses the positive values of the anomalous conductivities as explained in [58]. The  $\sigma_{ij}^A$  for all orientations manifests a monotonic, almost linear increase with decreasing temperature. At 2 K, the AHC values in our samples reach a maximum of  $340 \Omega^{-1} \text{ cm}^{-1}$  for  $\sigma_{xy}^A$ ,  $263 \Omega^{-1} \text{ cm}^{-1}$  for  $\sigma_{zx}^A$ , and  $296 \Omega^{-1} \text{ cm}^{-1}$  for  $\sigma_{zy}^A$ . These values are in very good agreement with

values of  $\sigma_{ij}^A \approx 200 \Omega^{-1} \text{ cm}^{-1}$ ,  $\sigma_{xy}^A \approx 350 \Omega^{-1} \text{ cm}^{-1}$ , and  $\sigma_{zx}^A \approx 260 \Omega^{-1} \text{ cm}^{-1}$  reported in Refs. [15,42,43] for the lowest temperatures. However, the most notable is the contrasting difference in the temperature behavior of the anomalous Hall conductivity of our samples and those studied in Refs. [15,42,43], which show a nearly temperature-independent behavior of AHC upon cooling from 250 down to 150 K followed by a strong decrease below 150 K. The reason for the different temperature dependence of the anomalous Hall effect is unclear and may be related to the different off-stoichiometry of the samples prepared by different methods.

### C. *Ab initio* calculations of anomalous Hall conductivity and Berry curvature

In order to gain further insight into the observed conductivity anisotropy, we have performed *ab initio* calculations of the Berry curvature ( $\Omega^y$ ) and AHC. The results are shown in Fig. 5.

As one can see, there is a noticeable difference between the shapes of  $\sigma_{xy}(E)$  and  $\sigma_{yz}(E)$  [Fig. 5(a)], indicating a significant anisotropy for moments along the  $\mathbf{a}$  ( $\mathbf{M}||\mathbf{100}$ ) and  $\mathbf{c}$  axes ( $\mathbf{M}||\mathbf{001}$ ). We find a higher value for  $\sigma_{yz} = 521 \Omega^{-1} \text{ cm}^{-1}$  than for  $\sigma_{xy} = 479 \Omega^{-1} \text{ cm}^{-1}$ , which is in disagreement with our experimental findings. Note that our calculations were performed using the perfect stoichiometry  $\text{Fe}_3\text{Sn}$  unlike the measurements performed on the experimental samples  $\text{Fe}_{3+\delta}\text{Sn}_{1-\delta}$ , with  $\delta = 0.02, 0.03$ . The theoretical values of AHC depend on the accuracy of the computed position of the Fermi level. In fact, as seen in Fig. 5(a),  $\sigma_{xy}(E)$  and  $\sigma_{xz}(E)$  cross just below the Fermi energy, hence slight hole doping would lead to  $\sigma_{xy} > \sigma_{xz}$ , in the vicinity of Fermi level, as observed experimentally. This sensitivity of the Hall conductivities to the stoichiometry of samples may cause the difference between the experimental results reported here and in Refs. [15,42,43]. On theoretical side, the inclusion of substitution disorder (the presence of  $\delta$ ) even at the simplest level (e.g., virtual crystal approximation [59]) would lead to a shift of the Fermi level and consequently to a qualitatively different anisotropy of AHC.

Additional information concerning the origin of the AHC anisotropy is obtained looking at the Berry curvature distribution in the Brillouin zone (BZ). This was done by scanning the entire BZ and calculating Berry curvature within  $(k_x, k_y)$  planes at different  $k_z$  values. A similar strategy was also employed in Ref. [15]. By doing so, we were able to identify a region of  $k_z$  values, roughly  $0.05 \leq k_z \leq 0.13$ , in which there is a dominant contribution of the positive values of the Berry curvature. Figures 5(b) and 5(c) depict Berry curvature distribution in the  $(k_x, k_y)$  plane at  $k_z = 0.11$ . When magnetization is set along the  $\mathbf{c}$  axis, typical features of the  $\Omega^z$  include a large positive contribution in the vicinity of the  $\Gamma$  point as well as the appearance of the hotspots at the BZ boundaries ( $U_1^* - U_6^*$  points in Ref. [15]), Fig. 5(b). In the case of magnetization along the  $\mathbf{a}$  axis, we observe even larger hotspots of positive  $\Omega^x$  component of the Berry curvature at the BZ boundaries, Fig. 5(c). The main qualitative difference is the absence of the large contribution in the vicinity of the BZ center that was present when the magnetization was set along the  $\mathbf{c}$  axis. Such difference in the Berry curvature distribution for two

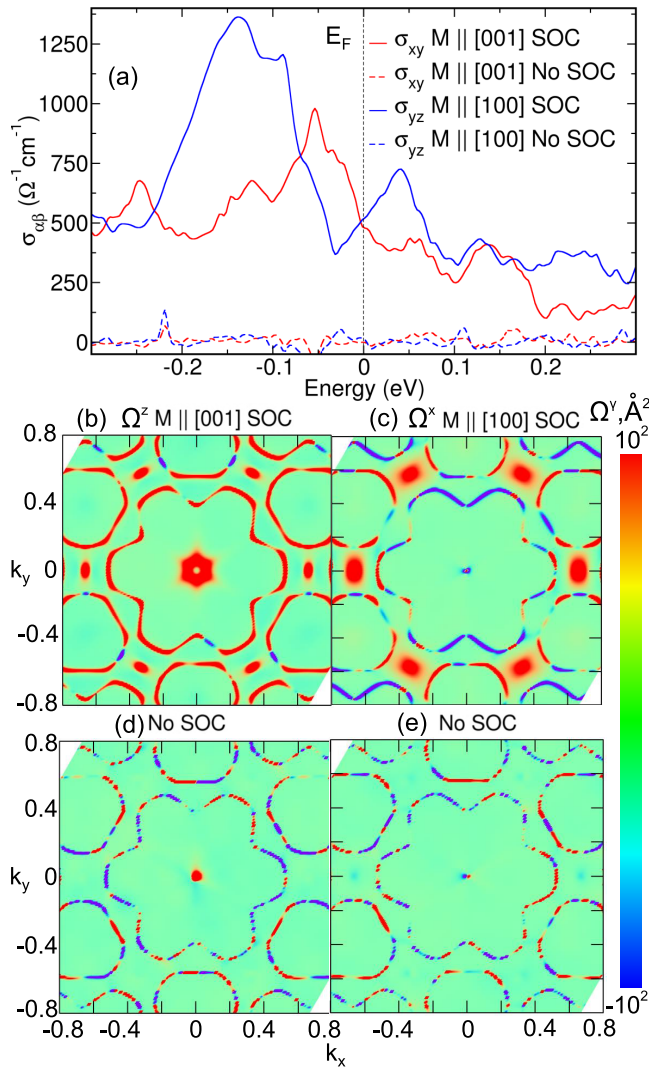


FIG. 5. Calculated AHC (a) and Berry curvature with (b), (c) and without (d), (e) SOC in  $\text{Fe}_3\text{Sn}$ . Red and blue colors in (b)–(e) indicate the positive and negative values of the  $\gamma$  component of the Berry curvature  $\Omega^y$ , respectively. The  $(k_x, k_y)$  cuts were made at  $k_z = 0.11$ .

different magnetization orientations signals an intrinsic origin of the observed anisotropy in the anomalous Hall effect of  $\text{Fe}_3\text{Sn}$ . At the same time, this also reflects the sensitivity of the electronic states to the magnetization direction, i.e., indicating the reconstruction of the band structure driven by an external magnetic field.

#### D. Anisotropic charge transport

In this section we discuss the anisotropic charge transport properties of single-crystalline  $\text{Fe}_{3+\delta}\text{Sn}_{1-\delta}$  (with  $\delta = 0.02$  and  $0.03$ ) in relation with the numerical calculations. Figure 6(a) shows the temperature dependence of the anisotropy ratio for the longitudinal resistivity  $\rho_{xx}/\rho_{zz}$  and the anomalous Hall resistivity  $\rho_{xy}^A/\rho_{zy}^A$ . The anisotropy ratio  $\rho_{xx}/\rho_{zz}$  exhibits a nonmonotonic dependence with temperature revealing a broad maximum at around 150 K, Fig. 6(a). At this temperature, the ratio  $\rho_{xx}/\rho_{zz} \approx 3$  and decreases to about 2.7 at both higher (300 K) and lower (2 K) temperatures.

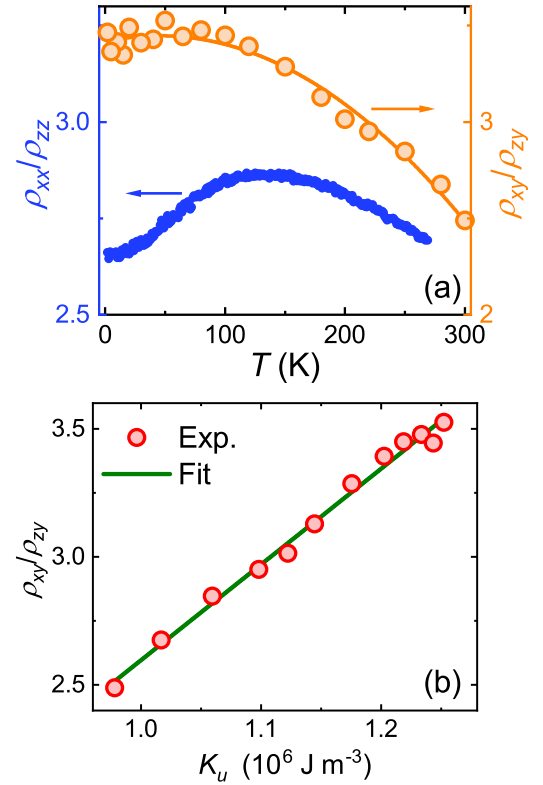


FIG. 6. Temperature dependence of the anisotropy ratio of the longitudinal resistivity  $\rho_{xx}/\rho_{zz}$  (blue scale) and of the anomalous Hall resistivity  $\rho_{xy}^A/\rho_{zy}^A$  (orange scale) for single-crystalline  $\text{Fe}_{3+\delta}\text{Sn}_{1-\delta}$ , (a). (b) The anisotropy ratio of anomalous Hall resistivity  $\rho_{xy}^A/\rho_{zy}^A$  vs uniaxial anisotropy constant  $K_u$ , reproduced from Ref. [40]. Green line represents the linear fit to the experimental data.

This indicates the difference in the transition region for the longitudinal in-plane and interplane transport, in which the electron-electron scattering is suppressed by the scattering on phonons.

It is necessary to note that the “anomalous” anisotropy of the longitudinal resistivity, namely that the interlayer resistivity is smaller than the intralayer one, has been already reported for the other kagome magnets, e.g., paramagnetic  $\text{CoSn}$  and  $\text{YCr}_6\text{Ge}_6$  [27,34], chiral antiferromagnets  $\text{Mn}_3\text{X}$  ( $X = \text{Sn}, \text{Ge}$ ) [10,60], spin-spiral  $\text{YMn}_6\text{Sn}_4\text{Ge}_2$  [35], spin-ice  $\text{HoAgGe}$  [18], antiferromagnetic  $\text{FeSn}$  [32,61], and ferromagnetic  $\text{Fe}_3\text{Sn}_2$  [33]. The origin of this phenomena is not yet settled. Huang *et al.* [27] proposed that the anisotropy in the longitudinal resistivity of  $\text{CoSn}$  is due to the existence of flat-band electronic states with large effective masses and suppressed kinetic energy within the kagome layers. On the other hand, Sales *et al.* [32] suggested an enhanced conductivity along the  $\mathbf{c}$  axis through the Sn ions. An alternative explanation for the anisotropic conductivity in  $\text{FeSn}$  was recently proposed in Ref. [61]. In  $\text{FeSn}$ , it was suggested that the anisotropy of optical conductivity for both the in-plane and interplane polarization is dominated by interlayer transitions between kagome layers through the adjacent Sn-buffer layers. Interestingly, previous electronic band-structure calculation for  $\text{FeSn}$  and  $\text{Fe}_3\text{Sn}_2$  also reported the presence of flat bands [5,62], which supports the proposal of Huang *et al.* [27].

However, our band-structure calculations, as well as previous ones for Fe<sub>3</sub>Sn [15,41,42] did not reveal such flat bands in the vicinity of the Fermi level. Moreover, as one can see in Fig. 1(d), Fe<sub>3</sub>Sn does not have a Sn-buffer plane, while the conductivity through Sn ions is less probable due to large Sn-Sn distance as shown for the related compound FeSn in Ref. [61]. Additional studies are necessary to reveal the origin of the conductivity anisotropy.

We found that ratios of the anomalous Hall resistivities  $\rho_{xy}/\rho_{zy}$  and  $\rho_{xx}/\rho_{zz}$  exhibit different temperature dependencies, in Fig. 6(a). The experimental temperature dependence of  $K_u$  was also reported previously [40], thus the almost-linear functional dependence  $\rho_{xy}/\rho_{zy}[K_u]$  has temperature as implicit parameter Fig. 6(b). This relation suggests that the large value of the anomalous Hall resistivity is governed by the spin-orbit coupling (which is the largest within the Fe-Sn kagome metals family [40]) besides the nontrivial temperature dependence.

To demonstrate the contribution of spin-orbit coupling to the large anomalous Hall effect in Fe<sub>3</sub>Sn we investigate the role of the SOC in the contributions to the Berry curvature and, consequently, in the observed anisotropy in the anomalous Hall effect. For this reason we perform an additional set of calculations with SOC turned off. The resulting AHC is shown in Fig. 5(a) (dashed lines), and the corresponding Berry curvature distribution is depicted in Figs. 5(d) and 5(e). As one can see, the SOC itself is not necessary to produce nonzero contributions to the Berry curvature, Figs. 5(d) and 5(e). The key observation here is that, although the Berry curvature is not zero everywhere, there are roughly equal contributions of positive and negative values, which when integrated produce nearly zero Hall conductivity, Fig. 5(a). The inclusion of the SOC leads to the appearance of large, uncompensated hot-spots of positive values of the Berry curvature, which then translates into a finite anomalous conductivity.

Our final remark concerns the origin of the anomalous Hall conductivity in Fe<sub>3</sub>Sn. The large (nonzero) value of the residual anomalous Hall resistivity observed in our study and also in Refs. [15,42,43] suggests a significant extrinsic contribution to AHC due to disorder and impurities. On the other hand, large residual anomalous Hall resistivity was also reported for related kagome metals Fe<sub>5</sub>Sn<sub>3</sub> and Fe<sub>3</sub>Sn<sub>2</sub> and attributed to the intrinsic mechanism of AHE [33,63]. Our results also indicate that the contribution to the AHE of the quadratic term related to the Berry curvature is larger for the interplane transport, Fig. 3(d). The latter is also visible in the less pronounced temperature-dependent character of  $\sigma_{zy}^A$  compared to  $\sigma_{xy}^A$ , Fig. 4(a). In addition, the extrapolation of the low-temperature part of AHC gives the values of  $\sigma_{xy}^A = 240 \Omega^{-1} \text{ cm}^{-1}$  and  $\sigma_{zy}^A = 210 \Omega^{-1} \text{ cm}^{-1}$ , once again demonstrating that the relative contribution of the intrinsic Hall effect dominates for fields applied in the kagome plane. Our attempts to separate the intrinsic and extrinsic contri-

butions to the anomalous Hall conductivity using existing scaling approaches [64–66] were not conclusive. Moreover, to quantify the contribution of the different scattering mechanisms, e.g., skew scattering, side jump and intrinsic (Berry curvature), it is important to clarify whether these mechanisms cooperate or compete. Therefore, the separation of different contributors to the anomalous charge transport remains a challenging task. More reliable information can be provided by the optical Hall conductivity studies that identify the interband transitions directly contributing to the intrinsic AHE.

#### IV. CONCLUSIONS

In summary, our experimental study of the longitudinal resistivity and Hall effect in single crystals of Fe<sub>3+ $\delta$</sub> Sn<sub>1- $\delta$</sub>  ( $\delta = 0.02$  and  $0.03$ ) revealed peculiar anisotropic behavior in charge transport. We found that the longitudinal interplane resistivity, measured with the current  $\mathbf{I}$  applied along  $\mathbf{c}$  axis, is about three times lower compared to the resistivity in the kagome  $ab$  plane. The ordinary Hall constant ( $R_0$ ) has a negative sign for  $\mathbf{I}||\mathbf{a}$  and a positive sign for  $\mathbf{I}||\mathbf{c}$ . The anomalous Hall resistivity exhibits significant anisotropy with  $\rho_{xy}^A = 8 \mu\Omega \text{ cm}$  and  $\rho_{zy}^A = 3.2 \mu\Omega \text{ cm}$  at 300 K. With decreasing temperature, the anisotropy ratio ( $\rho_{xy}^A / \rho_{zy}^A$ ) increases with about 40%. The off-diagonal anomalous Hall conductivity shows a monotonic increase with decreasing temperature and at 2 K reaches  $\sigma_{xy}^A = 340 \Omega^{-1} \text{ cm}^{-1}$  and  $\sigma_{zy}^A = 263 \Omega^{-1} \text{ cm}^{-1}$ . We found that the anisotropy ratio ( $\rho_{xy}^A / \rho_{zy}^A$ ) scales almost linear with the magnetocrystalline anisotropy constant ( $K_u$ ) in the temperature range  $2 \text{ K} \leq T \leq 300 \text{ K}$ , indicating that the spin-orbit coupling provides a common mechanism for the anisotropic charge transport as well as the magnetocrystalline anisotropy energy. The importance of the SOC in the AHC is further established by the material specific *ab initio* simulations. The anisotropy of the anomalous Hall effect is found to originate from two qualitatively different distributions of the Berry curvature for the in-plane ( $\mathbf{M}||\mathbf{a}$ ) and out-of-plane ( $\mathbf{M}||\mathbf{c}$ ) orientations of magnetization ( $\mathbf{M}$ ). The magnetic reconstruction of bands near the Fermi level, due to the SOC, seems to be largely responsible for the observed behavior of the Berry curvature, and, consequently, the large anomalous Hall effect in Fe<sub>3</sub>Sn.

#### ACKNOWLEDGMENTS

This work was supported by the Deutsche Forschungsgemeinschaft (DFG, German Research Foundation) TRR 360-492547816 and Project No. ANCD 20.80009.5007.19 (Moldova). L.C. acknowledges the hospitality of Clarendon Laboratory, Department of Physics, University of Oxford, UK, during the final preparation of the manuscript.

- [1] L. Balents, Spin liquids in frustrated magnets, *Nature (London)* **464**, 199 (2010).  
 [2] C. Broholm, R. J. Cava, S. A. Kivelson, D. G. Nocera, M. R. Norman, and T. Senthil, Quantum spin liquids, *Science* **367**, eaay0668 (2020).

- [3] G. Xu, B. Lian, and S.-C. Zhang, Intrinsic quantum anomalous Hall effect in the kagome lattice Cs<sub>2</sub>LiMn<sub>3</sub>F<sub>12</sub>, *Phys. Rev. Lett.* **115**, 186802 (2015).  
 [4] J.-X. Yin, S. S. Zhang, H. Li, K. Jiang, G. Chang, B. Zhang, B. Lian, C. Xiang, I. Belopolski, H. Zheng *et al.*,



- Giant and anisotropic many-body spin-orbit tunability in a strongly correlated kagome magnet, *Nature (London)* **562**, 91 (2018).
- [5] M. Kang, L. Ye, S. Fang, J.-S. You, A. Levitan, M. Han, J. I. Facio, C. Jozwiak, A. Bostwick, E. Rotenberg *et al.*, Dirac fermions and flat bands in the ideal kagome metal FeSn, *Nat. Mater.* **19**, 163 (2020).
- [6] D. F. Liu, A. J. Liang, E. K. Liu, Q. N. Xu, Y. W. Li, C. Chen, D. Pei, W. J. Shi, S. K. Mo, P. Dudin *et al.*, Magnetic Weyl semimetal phase in a Kagomé crystal, *Science* **365**, 1282 (2019).
- [7] J.-X. Yin, B. Lian, and M. Z. Hasan, Topological kagome magnets and superconductors, *Nature (London)* **612**, 647 (2022).
- [8] B. R. Ortiz, S. M. L. Teicher, Y. Hu, J. L. Zuo, P. M. Sarte, E. C. Schueller, A. M. M. Abeykoon, M. J. Krogstad, S. Rosenkranz, R. Osborn, R. Seshadri, L. Balents, J. He, and S. D. Wilson, CsV<sub>3</sub>Sb<sub>5</sub>: A Z<sub>2</sub> Topological kagome metal with a superconducting ground state, *Phys. Rev. Lett.* **125**, 247002 (2020).
- [9] P. E. Siegfried, H. Bhandari, D. C. Jones, M. P. Ghimire, R. L. Dally, L. Poudel, M. Bleuel, J. W. Lynn, I. I. Mazin, and N. J. Ghimire, Magnetization-driven Lifshitz transition and charge-spin coupling in the kagome metal YMn<sub>6</sub>Sn<sub>6</sub>, *Commun. Phys.* **5**, 58 (2022).
- [10] N. Kiyohara, T. Tomita, and S. Nakatsuji, Giant anomalous Hall effect in the chiral antiferromagnet Mn<sub>3</sub>Ge, *Phys. Rev. Appl.* **5**, 064009 (2016).
- [11] A. K. Nayak, J. E. Fischer, Y. Sun, B. Yan, J. Karel, A. C. Komarek, C. Shekhar, N. Kumar, W. Schnelle, J. Kübler *et al.*, Large anomalous Hall effect driven by a nonvanishing Berry curvature in the noncolinear antiferromagnet Mn<sub>3</sub>Ge, *Sci. Adv.* **2**, e1501870 (2016).
- [12] E. Liu, Y. Sun, N. Kumar, L. Muechler, A. Sun, L. Jiao, S.-Y. Yang, D. Liu, A. Liang, Q. Xu *et al.*, Giant anomalous Hall effect in a ferromagnetic kagome-lattice semimetal, *Nat. Phys.* **14**, 1125 (2018).
- [13] L. Ye, M. Kang, J. Liu, F. von Cube, C. R. Wicker, T. Suzuki, C. Jozwiak, A. Bostwick, E. Rotenberg, D. C. Bell *et al.*, Massive Dirac fermions in a ferromagnetic kagome metal, *Nature (London)* **555**, 638 (2018).
- [14] H. Yang, W. You, J. Wang, J. Huang, C. Xi, X. Xu, C. Cao, M. Tian, Z.-A. Xu, J. Dai, and Y. Li, Giant anomalous Nernst effect in the magnetic Weyl semimetal Co<sub>3</sub>Sn<sub>2</sub>S<sub>2</sub>, *Phys. Rev. Mater.* **4**, 024202 (2020).
- [15] T. Chen, S. Minami, A. Sakai, Y. Wang, Z. Feng, T. Nomoto, M. Hirayama, R. Ishii, T. Koretsune, R. Arita, and S. Nakatsuji, Large anomalous Nernst effect and nodal plane in an iron-based kagome ferromagnet, *Sci. Adv.* **8**, abk1480 (2022).
- [16] F. Schilberth, N. Unglert, L. Prodan, F. Meggle, J. Ebad Allah, C. A. Kuntscher, A. A. Tsirlin, V. Tsurkan, J. Deisenhofer, L. Chioncel, I. Kézsmárki, and S. Bordács, Magneto-optical detection of topological contributions to the anomalous Hall effect in a kagome ferromagnet, *Phys. Rev. B* **106**, 144404 (2022).
- [17] F. Schilberth, M.-C. Jiang, S. Minami, M. A. Kassem, F. Mayr, T. Koretsune, Y. Tabata, T. Waki, H. Nakamura, G.-Y. Guo, R. Arita, I. Kézsmárki, and S. Bordács, Nodal-line resonance generating the giant anomalous Hall effect of Co<sub>3</sub>Sn<sub>2</sub>S<sub>2</sub>, *Phys. Rev. B* **107**, 214441 (2023).
- [18] K. Zhao, H. Deng, H. Chen, K. A. Ross, V. Petříček, G. Günther, M. Russina, V. Hutanu, and P. Gegenwart, Realization of the kagome spin ice state in a frustrated intermetallic compound, *Science* **367**, 1218 (2020).
- [19] Z. Hou, W. Ren, B. Ding, G. Xu, Y. Wang, B. Yang, Q. Zhang, Y. Zhang, E. Liu, F. Xu *et al.*, Observation of various and spontaneous magnetic skyrmionic bubbles at room temperature in a frustrated kagome magnet with uniaxial magnetic anisotropy, *Adv. Mater.* **30**, 201706306 (2018).
- [20] M. Hirschberger, T. Nakajima, S. Gao, L. Peng, A. Kikkawa, T. Kurumaji, M. Kriener, Y. Yamasaki, H. Sagayama, H. Nakao *et al.*, Skyrmion phase and competing magnetic orders on a breathing kagomé lattice, *Nat. Commun.* **10**, 5831 (2019).
- [21] M. Althaler, E. Lysne, E. Roede, L. Prodan, V. Tsurkan, M. A. Kassem, H. Nakamura, S. Krohns, I. Kézsmárki, and D. Meier, Magnetic and geometric control of spin textures in the itinerant kagome magnet Fe<sub>3</sub>Sn<sub>2</sub>, *Phys. Rev. Res.* **3**, 043191 (2021).
- [22] J.-X. Yin, S. S. Zhang, G. Chang, Q. Wang, S. S. Tsirkin, Z. Guguchia, B. Lian, H. Zhou, K. Jiang, I. Belopolski *et al.*, Negative flat band magnetism in a spin-orbit-coupled correlated kagome magnet, *Nat. Phys.* **15**, 443 (2019).
- [23] J. Watanabe, Y. Araki, K. Kobayashi, A. Ozawa, and K. Nomura, Magnetic orderings from spin-orbit coupled electrons on kagome lattice, *J. Phys. Soc. Jpn.* **91**, 083702 (2022).
- [24] N. Nagaosa, J. Sinova, S. Onoda, A. H. MacDonald, and N. P. Ong, Anomalous Hall effect, *Rev. Mod. Phys.* **82**, 1539 (2010).
- [25] S. N. Guin, P. Vir, Y. Zhang, N. Kumar, S. J. Watzman, C. Fu, E. Liu, K. Manna, W. Schnelle, J. Gooth *et al.*, Zero-field nernst effect in a ferromagnetic kagome-lattice Weyl semimetal Co<sub>3</sub>Sn<sub>2</sub>S<sub>2</sub>, *Adv. Mater.* **31**, 1806622 (2019).
- [26] X. Li, J. Koo, Z. Zhu, K. Behnia, and B. Yan, Field-linear anomalous Hall effect and Berry curvature induced by spin chirality in the kagome antiferromagnet Mn<sub>3</sub>Sn, *Nat. Commun.* **14**, 1642 (2023).
- [27] H. Huang, L. Zheng, Z. Lin, X. Guo, S. Wang, S. Zhang, C. Zhang, Z. Sun, Z. Wang, H. Weng, L. Li, T. Wu, X. Chen, and C. Zeng, Flat-band-induced anomalous anisotropic charge transport and orbital magnetism in kagome metal CoSn, *Phys. Rev. Lett.* **128**, 096601 (2022).
- [28] D. C. Johnston, The puzzle of high temperature superconductivity in layered iron pnictides and chalcogenides, *Adv. Phys.* **59**, 803 (2010).
- [29] Y. Wang, C. Xian, J. Wang, B. Liu, L. Ling, L. Zhang, L. Cao, Z. Qu, and Y. Xiong, Anisotropic anomalous Hall effect in triangular itinerant ferromagnet Fe<sub>3</sub>GeTe<sub>2</sub>, *Phys. Rev. B* **96**, 134428 (2017).
- [30] T. Asaba, S. M. Thomas, M. Curtis, J. D. Thompson, E. D. Bauer, and F. Ronning, Anomalous Hall effect in the kagome ferrimagnet GdMn<sub>6</sub>Sn<sub>6</sub>, *Phys. Rev. B* **101**, 174415 (2020).
- [31] Y. Xiang, Q. Li, Y. Li, W. Xie, H. Yang, Z. Wang, Y. Yao, and H.-H. Wen, Twofold symmetry of c-axis resistivity in topological kagome superconductor CsV<sub>3</sub>Sb<sub>5</sub> with in-plane rotating magnetic field, *Nat. Commun.* **12**, 6727 (2021).
- [32] B. C. Sales, J. Yan, W. R. Meier, A. D. Christianson, S. Okamoto, and M. A. McGuire, Electronic, magnetic, and thermodynamic properties of the kagome layer compound FeSn, *Phys. Rev. Mater.* **3**, 114203 (2019).



- [33] Q. Du, Z. Hu, M.-G. Han, F. Camino, Y. Zhu, and C. Petrovic, Topological Hall effect anisotropy in kagome bilayer metal  $\text{Fe}_3\text{Sn}_2$ , *Phys. Rev. Lett.* **129**, 236601 (2022).
- [34] T. Y. Yang, Q. Wan, J. P. Song, Z. Du, J. Tang, Z. W. Wang, N. C. Plumb, M. Radovic, G. W. Wang, G. Y. Wang *et al.*, Fermi-level flat band in a kagome magnet, *Quantum Front.* **1**, 14 (2022).
- [35] H. Bhandari, R. L. Dally, P. E. Siegfried, R. B. Regmi, K. C. Rule, S. Chi, J. W. Lynn, I. I. Mazin, and N. J. Ghimire, Magnetism and fermiology of kagome magnet  $\text{YMn}_6\text{Sn}_4\text{Ge}_2$ , *npj Quantum Mater.* **9**, 6 (2024).
- [36] Y. Zhang, Y. Sun, H. Yang, J. Železný, S. P. P. Parkin, C. Felser, and B. Yan, Strong anisotropic anomalous Hall effect and spin Hall effect in the chiral antiferromagnetic compounds  $\text{Mn}_3\text{X}$  ( $X = \text{Sn, Ga, Ir, Rh, and Pt}$ ), *Phys. Rev. B* **95**, 075128 (2017).
- [37] L. Song, F. Zhou, H. Li, B. Ding, X. Li, X. Xi, Y. Yao, Y. Lau, and W. Wang, Large anomalous Hall effect at room temperature in a fermi-level-tuned kagome antiferromagnet, *Adv. Funct. Mater.* **34**, 2316588 (2024).
- [38] G. Dhakal, F. Cheenicode Kabeer, A. K. Pathak, F. Kabir, N. Poudel, R. Filippone, J. Casey, A. Pradhan Sakhya, S. Regmi, C. Sims, K. Dimitri, P. Manfrinetti, K. Gofryk, P. M. Oppeneer, and M. Neupane, Anisotropically large anomalous and topological Hall effect in a kagome magnet, *Phys. Rev. B* **104**, L161115 (2021).
- [39] H. Li, B. Ding, J. Chen, Z. Li, E. Liu, X. Xi, G. Wu, and W. Wang, Large anisotropic topological Hall effect in a hexagonal non-collinear magnet  $\text{Fe}_5\text{Sn}_3$ , *Appl. Phys. Lett.* **116**, 182405 (2020).
- [40] L. Prodan, D. M. Evans, S. M. Griffin, A. Östlin, M. Althaler, E. Lysne, I. G. Filippova, S. Shova, L. Chioncel, V. Tsurkan, and I. Kézsmárki, Large ordered moment with strong easy-plane anisotropy and vortex-domain pattern in the kagome ferromagnet  $\text{Fe}_3\text{Sn}$ , *Appl. Phys. Lett.* **123**, 021901 (2023).
- [41] C. Shen, I. Samathrakris, K. Hu, H. K. Singh, N. Fortunato, H. Liu, O. Gutfleisch, and H. Zhang, Thermodynamical and topological properties of metastable  $\text{Fe}_3\text{Sn}$ , *npj Comput. Mater.* **8**, 248 (2022).
- [42] B. P. Belbase, L. Ye, B. Karki, J. I. Facio, J.-S. You, J. G. Checkelsky, J. van den Brink, and M. P. Ghimire, Large anomalous Hall effect in single crystals of the kagome Weyl ferromagnet  $\text{Fe}_3\text{Sn}$ , *Phys. Rev. B* **108**, 075164 (2023).
- [43] A. Low, S. Ghosh, S. Ghorai, and S. Thirupathaiah, Effect of electron-phonon scattering on the anomalous Hall conductivity of  $\text{Fe}_3\text{Sn}$ : A kagome ferromagnetic metal, *Phys. Rev. B* **108**, 094404 (2023).
- [44] G. Bosch, A Hall device in an integrated circuit, *Solid-State Electron.* **11**, 712 (1968).
- [45] P. Hohenberg and W. Kohn, Inhomogeneous electron gas, *Phys. Rev.* **136**, B864 (1964).
- [46] W. Kohn and L. J. Sham, Self-consistent equations including exchange and correlation effects, *Phys. Rev.* **140**, A1133 (1965).
- [47] P. E. Blöchl, Projector augmented-wave method, *Phys. Rev. B* **50**, 17953 (1994).
- [48] G. Kresse and J. Furthmüller, Efficiency of ab-initio total energy calculations for metals and semiconductors using a plane-wave basis set, *Comput. Mater. Sci.* **6**, 15 (1996).
- [49] G. Kresse and J. Furthmüller, Efficient iterative schemes for *ab initio* total-energy calculations using a plane-wave basis set, *Phys. Rev. B* **54**, 11169 (1996).
- [50] J. P. Perdew, A. Ruzsinszky, G. I. Csonka, O. A. Vydrov, G. E. Scuseria, L. A. Constantin, X. Zhou, and K. Burke, Restoring the density-gradient expansion for exchange in solids and surfaces, *Phys. Rev. Lett.* **100**, 136406 (2008).
- [51] N. Marzari and D. Vanderbilt, Maximally localized generalized Wannier functions for composite energy bands, *Phys. Rev. B* **56**, 12847 (1997).
- [52] A. A. Mostofi, J. R. Yates, G. Pizzi, Y.-S. Lee, I. Souza, D. Vanderbilt, and N. Marzari, An updated version of wannier90: A tool for obtaining maximally-localised Wannier functions, *Comput. Phys. Commun.* **185**, 2309 (2014).
- [53] Q. Wu, S. Zhang, H.-F. Song, M. Troyer, and A. A. Soluyanov, Wanniertools: An open-source software package for novel topological materials, *Comput. Phys. Commun.* **224**, 405 (2018).
- [54] X. Wang, J. R. Yates, I. Souza, and D. Vanderbilt, *Ab initio* calculation of the anomalous Hall conductivity by Wannier interpolation, *Phys. Rev. B* **74**, 195118 (2006).
- [55] Q. Wang, S. Sun, X. Zhang, F. Pang, and H. Lei, Anomalous Hall effect in a ferromagnetic  $\text{Fe}_3\text{Sn}_2$  single crystal with a geometrically frustrated Fe bilayer kagome lattice, *Phys. Rev. B* **94**, 075135 (2016).
- [56] N. Kumar, Y. Soh, Y. Wang, and Y. Xiong, Magnetotransport as a diagnostic of spin reorientation: Kagome ferromagnet as a case study, *Phys. Rev. B* **100**, 214420 (2019).
- [57] B. Raquet, M. Viret, E. Sondergard, O. Céspedes, and R. Mamy, Electron-magnon scattering and magnetic resistivity in 3d ferromagnets, *Phys. Rev. B* **66**, 024433 (2002).
- [58] The AHC was calculated from the longitudinal and anomalous Hall resistivities measured for different configurations. Considering the anisotropic behavior of longitudinal resistivities,  $\rho_{xx} \neq \rho_{zz}$ , we have used the relation  $\sigma_{xy}^A = \rho_{xy}^A / [\rho_{xx}^2 + (\rho_{xy}^A)^2]$  for the in-plane ( $\mathbf{J} \parallel \mathbf{a}$ ,  $\mathbf{H} \parallel \mathbf{c}$ ) and  $\sigma_{zx}^A = \rho_{zx}^A / [\rho_{xx} \rho_{zz} + (\rho_{zx}^A)^2]$  for the cross-plane ( $\mathbf{J} \parallel \mathbf{c}$ ,  $\mathbf{H} \parallel \mathbf{a}$ ) configurations, respectively.
- [59] L. Bellaïche and D. Vanderbilt, Virtual crystal approximation revisited: Application to dielectric and piezoelectric properties of perovskites, *Phys. Rev. B* **61**, 7877 (2000).
- [60] A. Low, S. Ghosh, S. Changdar, S. Routh, S. Purwar, and S. Thirupathaiah, Tuning of topological properties in the strongly correlated antiferromagnet  $\text{Mn}_3\text{Sn}$  via Fe doping, *Phys. Rev. B* **106**, 144429 (2022).
- [61] J. Ebad-Allah, M.-C. Jiang, R. Borkenhagen, F. Meggle, L. Prodan, V. Tsurkan, F. Schilberth, G.-Y. Guo, R. Arita, I. Kézsmárki, and C. A. Kuntscher, Optical anisotropy of the kagome magnet  $\text{FeSn}$ : Dominant role of excitations between kagome and Sn layers, *Phys. Rev. B* **109**, L201106 (2024).
- [62] Z. Lin, J.-H. Choi, Q. Zhang, W. Qin, S. Yi, P. Wang, L. Li, Y. Wang, H. Zhang, Z. Sun, L. Wei, S. Zhang, T. Guo, Q. Lu, J.-H. Cho, C. Zeng, and Z. Zhang, Flatbands and emergent ferromagnetic ordering  $\text{Fe}_3\text{Sn}_2$  kagome lattices, *Phys. Rev. Lett.* **121**, 096401 (2018).
- [63] H. Li, B. Zhang, J. Liang, B. Ding, J. Chen, J. Shen, Z. Li, E. Liu, X. Xi, G. Wu, Y. Yao, H. Yang, and

- W. Wang, Large anomalous Hall effect in a hexagonal ferromagnetic  $\text{Fe}_5\text{Sn}_3$  single crystal, *Phys. Rev. B* **101**, 140409(R) (2020).
- [64] Y. Tian, L. Ye, and X. Jin, Proper scaling of the anomalous Hall effect, *Phys. Rev. Lett.* **103**, 087206 (2009).
- [65] D. Hou, G. Su, Y. Tian, X. Jin, S. A. Yang, and Q. Niu, Multi-variable scaling for the anomalous Hall effect, *Phys. Rev. Lett.* **114**, 217203 (2015).
- [66] L. Wu, K. Zhu, D. Yue, Y. Tian, and X. Jin, Anomalous Hall effect in localization regime, *Phys. Rev. B* **93**, 214418 (2016).